Supplementary Information

Spontaneous Oxidative Reconstruction of FeS_2 Speeds Up High-Efficiency Nitrate Reduction

Zhuo Wang,[a] Fei Wang,[a] Junjie Shao,[a,*] Wucan Huang,[a] Sujin Zhou,[a] Yijing Jiang,[a] Wenbiao Zhang[a,*] and Qingsheng Gao[a,*]

[a]College of Chemistry and Materials Science, Jinan University, Guangzhou 510632, P. R. China.

Emails: J.J.Shao@outlook.com (Junjie Shao); wbzhang@jnu.edu.cn (Wenbiao Zhang); tqsgao@jnu.edu.cn (Qingsheng Gao)

1. Supporting Methods

1.1 Materials and reagents

Potassium nitrate (KNO_3 99.0%) was purchased from Tianjin Fuchen Chemical Reagent Factory. Sodium borohydride ($NaBH_4$, 98%) was obtained from Sinopharm Chemical Reagent Co., Ltd. Ferrous sulfate heptahydrate ($FeSO_4·7H_2O$, 99.0%) and sublimed sulfur (S, 99.5%) were sourced from Tianjin Damao Chemical Reagent Factory. Ferric nitrate nonahydrate ($Fe(NO_3)_3·9H_2O$, 98.5%), potassium sulfate (K_2SO_4, AR 99.0%), urea (CH_4N_2O, AR 99%), sodium citrate dihydrate ($C_6H_5Na_3O_7·2H_2O$, AR 99.0%), sodium salicylate ($C_7H_6O_3$, 99.5%), sodium nitrite ($NaNO_2$, 99%), sodium nitroprusside dihydrate ($Na_2[Fe(CN)_5NO]·2H_2O$, 99.0%), p-Dimethylaminobenzaldehyde ($C_9H_{11}NO$, AR), N,N-dimethylformamide (C_3H_7NO, SP, 99.8%), N-methylpyrrolidone (C_5H_9NO, 99.5%), ethylene glycol ($C_2H_6O_2$, 99%), and ammonia solution (NH_3 in H_2O, electronic grade, 28wt%) were all acquired from Shanghai Macklin Biochemical Technology Co., sodium hydroxide (NaOH, 96.0%), Hydrochloric acid solution (HCl, 36.0-38.0 wt%), sodium hypochlorite solution (NaClO, 7.50%), and nitric acid (HNO_3, 65.0-68.0%) were procured from Guangzhou Chemical Reagent Factory, sodium hydroxide solution (NaOH, 50wt%) was obtained from ANPEL Laboratory Technologies (Shanghai) Inc., ethanol absolute (C_6H_5O, AR) was purchased from Guangdong Guanghua Sci-Tech Co.Ltd., PVDF (500 nm, the molecular weight is approximately 200,000). All chemicals were used as received without any further purification. All experiments were conducted using ultrapure water.

1.2 Catalyst preparation

Preparation of FeS_2: Dissolve $FeSO_4 \cdot 7H_2O$ (0.4 mmol, 0.111 g), sublimed sulfur (0.25 mmol, 0.08 g), and urea (2 mmol, 0.12 g) in a mixture of 6 mL DMF and 8 mL ethylene glycol in a reaction autoclave. Place the autoclave on a magnetic stirrer, stir the mixture under a nitrogen atmosphere for 0.5 hours, then add 1 mL of ammonia water. React the mixture at 160 °C for 12 hours in an oven to obtain a black precipitate. After the autoclave cools to room temperature, wash the product alternately with ethanol and deionized water six times. Then dry the black product in an oven at 60 °C. Finally, collect the black powder sample of FeS_2 by centrifugation.

Preparation of FeOOH: FeOOH was synthesized via a wet chemical method using sodium borohydride ($NaBH_4$) and iron (III) nitrate nonahydrate ($Fe(NO_3)_3 \cdot 9H_2O$) as precursors. 0.2 M $NaBH_4$ solution was slowly added dropwise into a 0.04 M $Fe(NO_3)_3 \cdot 9H_2O$ solution at 25 °C. The mixture was allowed to stand for 30 min, after which a yellowish-brown precipitate was collected by suction filtration. The resulting solid was washed and dried to obtain the final FeOOH powder product.

1.3 Physical characterizations

Powder X-ray diffraction (XRD) measurements were performed on a Rigaku MiniFlex600 X-ray diffractometer with Cu Kα radiation (40 kV, 30 mA). X-ray photoelectron spectroscopy (XPS) analysis was conducted on a Thermo Scientific K-Alpha + XPS spectrometer. Raman spectroscopy measurements were carried out using a LabRAM HR Evolution system (HORIBA France SAS). The scanning electron microscopy (SEM) images were acquired using a Hitachi SU1000 microscope. The

transmission electron microscopy (TEM) images and corresponding energy-dispersive X-ray spectroscopy mapping (EDS-mapping) were acquired using JEOL JEM-1400Flash and JEM-2100F microscopes. The online differential electrochemical mass spectrometry (DEMS) was using a LingLu Instruments QAS 100.

1.4 Electrochemical measurements

In a typical procedure, A homogeneous catalyst ink was obtained by subjecting a mixture of 5 mg electrocatalyst, 500 μL of 10% PVDF, and 1000 μL of anhydrous ethanol to ultrasonic treatment for 30 min. The resulting ink was then drop-cast onto a pre-treated carbon cloth substrate (1 cm × 2 cm).

All electrochemical measurements were conducted at 25 °C using a CHI660E electrochemical workstation (Shanghai Chenhua) in a standard three-electrode H-type electrolysis cell with 0.1 M K_2SO_4 as the electrolyte. The working electrode was a carbon cloth (1 cm × 2 cm, after hydrothermal treatment with concentrated nitric acid at 120 °C for 3 hours, rinse with ultrapure water until pH=7) loaded with 5 mg of catalyst, the reference electrode was a Hg/Hg_2Cl_2 electrode, and the counter electrode was a graphite rod. All measured potentials were converted to the reversible hydrogen electrode (RHE) scale using the following equation:

$$E\ vs.\ RHE = E\ vs.\ SCE\ + 0.0591 \times\ pH + 0.2414$$

Linear sweep voltammetry (LSV) polarization curves were recorded using a Hg/Hg_2Cl_2 reference electrode at a scan rate of 5.0 mV s^{-1} over the potential range from -1.4 to -0.2 V vs. RHE. Cyclic voltammetry (CV) measurements were performed at various scan rates (20, 40, 60, 80, and 100 mV/s) within the non-Faradaic region.

Electrochemical impedance spectroscopy (EIS) was carried out in a frequency range of 100 kHz to 0.01 Hz with an AC amplitude of 10 mV and a DC bias potential of -0.8 V vs. Hg/Hg_2Cl_2 reference electrode. Distribution of Relaxation Times (DRT) can be used to represent the impedance by an infinite number of infinitesimal differential RC-elements. The time constants of two main peaks (τ_1 and τ_2) need to be assigned to specific processes. Generally, the τ_1 peak at 10^2–10^0 s can be assigned to electron transfer (HER and eNO_3RR), whereas the τ_2 peak at 10^0 – 10^{-1} s can be attributed to the cation diffusion.[1-3]

1.5 Product analysis

UV-Vis spectrophotometer (Thermo Scientific GENESYS 10S UV-Vis) and ion chromatograph (IC, ICS-600, Thermo Fisher Scientiffic) with Dionex IonPac™ AS11-HC was used for analyzing concentration of NO_3^-, NO_2^-, NH_3 and N_2H_4.

Concentration of NH_3: the indophenol blue method was used for analyz.[4] Firstly, colorimetric reagent A (2 mL; containing 5 wt% salicylic acid and 5 wt% sodium citrate in 1.0 M NaOH solution) was mixed with the electrolyte sample (100 μL; diluted 100-fold with deionized water). Subsequently, colorimetric reagent B (0.05 mL; 0.05 M NaClO solution) and colorimetric reagent C (0.05 mL; 1 wt% sodium nitroprusside solution) were added to the mixture. The solution was protected from light and allowed to react for 1 hour at room temperature. The absorbance at 700 nm was then measured using a UV-Vis spectrophotometer.

Concentration of NO_3^- and NO_2^-: The quantitative analysis of reaction products by an external standard method for IC. Preparation of the eluent: Inject 500 μL of the

prepared 50% NaOH solution into ultrapure water and make up to 1800 mL. Ultrasonically exhaust for 30 min and then introduce nitrogen. Set the program to 40 min, the flow rate to 1.5 mL min^{-1}, and the injection volume to 10 μL.

Concentration of N_2H_4: Hydrazine was tested in accordance with the National Environmental Standard HJ 674-2013 of the People's Republic of China. Mix 0.2 mL *p*-dimethylaminobenzaldehyde (10 g L^{-1}, ethanol based) with 0.5 mL HCl (0.12 M) and stand for 20 min. Take 0.2 mL of hydrazine hydrate solution and dissolve it in 10mL of hydrochloric acid, then add water to make up to 1000 mL. Take 0.5 mL of the prepared hydrazine hydrate hydrochloric acid solution and add 1 mL of *p*-dimethylaminobenzaldehyde ethanol solution, standing in the dark for 20 min to observe. Usually, granular substances are produced. Just centrifuge and take the supernatant.

The substrate conversion, product selectivity, Faradaic efficiency, space-time yield and carbon balance were calculated based on the following equations (eq. 1 ~ 5):

$$Yield\ (\%) = \frac{mole\ of\ NH_3}{mole\ of\ NO_3^-\ substrate} \times 100\%\#(1)$$

$$Conversion\ (\%) = 1 - \frac{mole\ of\ NO_3^-\ remained}{mole\ of\ NO_3^-\ substrate} \times 100\ \%\#(2)$$

$$Selectivity\ (\%) = \frac{mole\ of\ NH_3}{mole\ of\ NO_3^-\ consumed} \times 100\%\#(3)$$

$$Faradaic\ efficiency\ (\%) = \frac{z \times mole\ of\ NH_3 \times F}{total\ charge\ passed} \times 100\%\#(4)$$

$$Space - time\ yield = \frac{mole\ of\ NH_3}{catalyst\ quality \times time}\#(5)$$

During eq. 4, z is the number of transferred electron, F is Faraday constant (96485 $C \cdot mol^{-1}$)

1.6 Theoretical calculation

The density functional theory (DFT) calculations were performed at the generalized gradient approximation (GGA) level within the Perdew–Burke–Emzerhof (PBE) functional using the CASTEP software implemented in Materials Studio. The total energy calculation was performed using a kinetic energy cutoff of 450.0 eV assigned to the plane-wave basis set for calculating the density of state. The self-consistent field (SCF) tolerance was 1×10^{-6} eV. The Brillouin zone was sampled by 5 × 5 × 1 k-points. The core electrons were replaced with ultrasoft pseudo-potentials. A vacuum thickness of 12 Å was choosen with using a five-layer 2 × 2 surface slab.

The binding energy (BE) of N-species (e.g. NO_3^-, NO_2^-, NH_3) was calculated as:

$$BE_{(\text{adsorbate})} = E_{(slab\ +\ \text{adsorbate})} - E_{(\text{slab})} - E_{(\text{adsorbate})}$$

$E_{(\text{slab+adsorbate})}$, $E_{(\text{slab})}$ and $E_{(\text{adsorbate})}$ are the energies of a slab with the adsorbate and the pure slab/facet and the adsorbate in the gas phase, respectively.

According to precious studies, the free energy change (ΔG) was computed using a computational hydrogen electrode model. For each step of eNO_3RR, ΔG was calculated as:

$$\Delta G = \Delta E + \Delta ZPE - T\Delta S$$

ΔE represents the difference in DFT energy, while ΔZPE and ΔS represent the zero-point energy and entropy between the reactants and products, respectively. T was set to 298.15 K in our work.

Preparation of Catalysts

Preparation of FeS_2

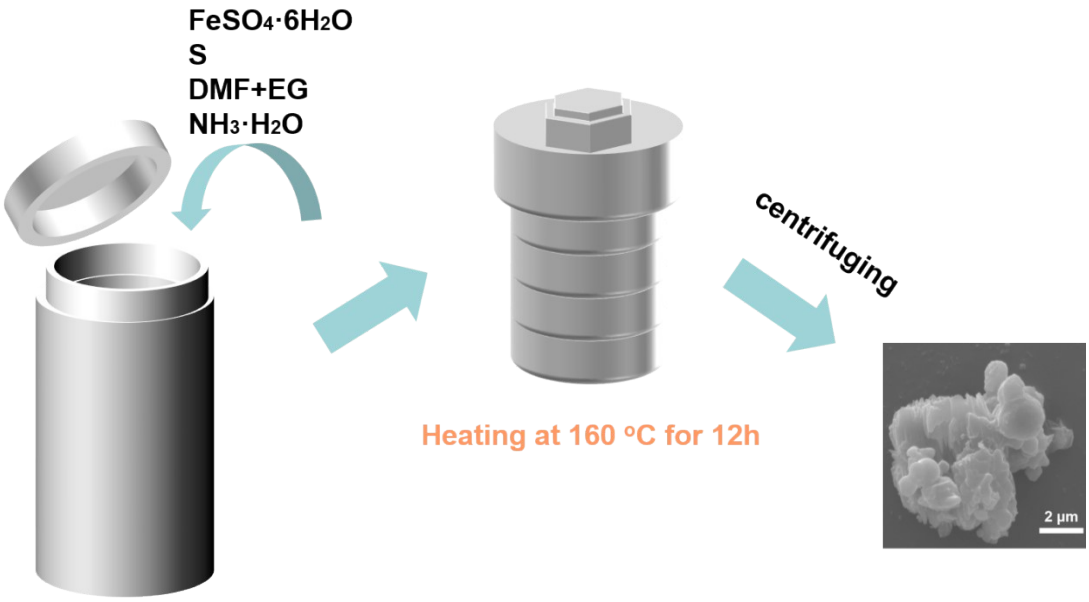

Fig. S1. Flowchart for the preparation of FeS_2.

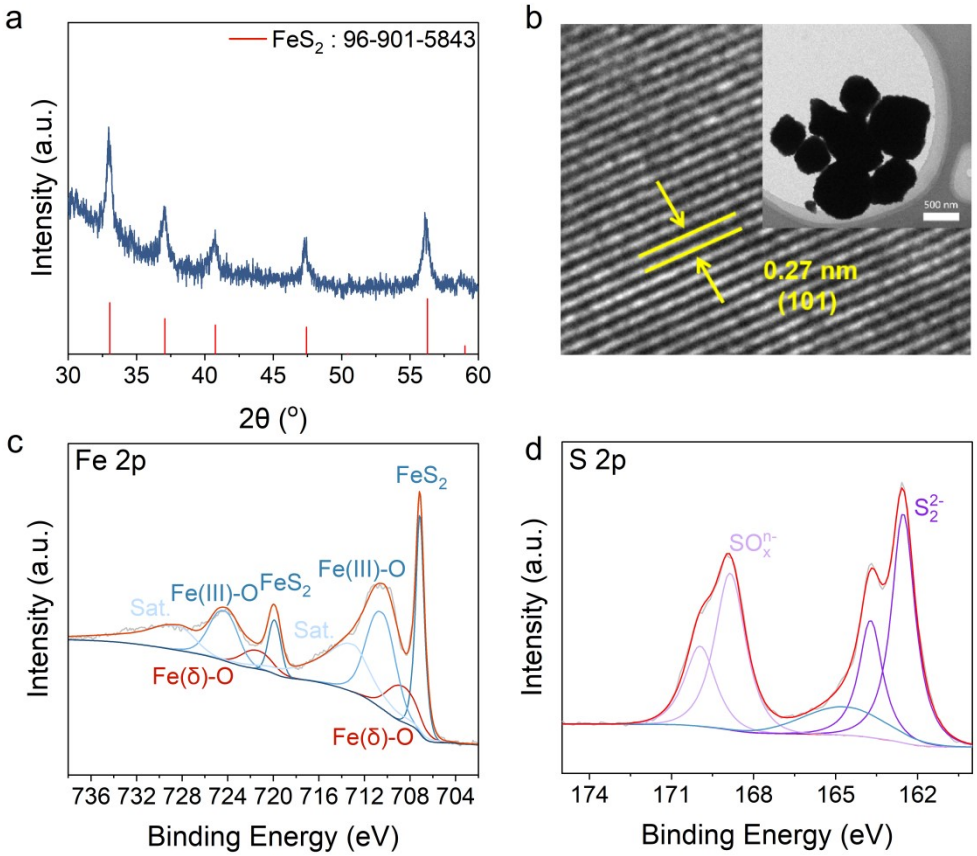

Fig. S2. (a) XRD pattern, (b) HRTEM image and XPS (c) Fe 2p, (d) S 2p spectra of FeS_2.

FeS_2 exhibits a pyrite-type structure belonging to the cubic crystal system **(Fig. S2a** and **S2b)**, which contributes to its favorable electrical conductivity for electrocatalytic applications. As depicted in Fe 2p profile (**Fig. S2c**), the peaks at 707.5 eV and 720.0 eV are assigned to Fe $2p_{3/2}$ and Fe $2p_{1/2}$, respectively. In the S 2p profile (**Fig. S2d**), two peaks are observed at 162.8 eV and 164.0 eV, corresponding to S $2p_{3/2}$ and $2p_{1/2}$, consistent with the characteristic spin–orbit splitting of pyrite. These results collectively confirm the successful formation of the FeS_2 phase.[5]

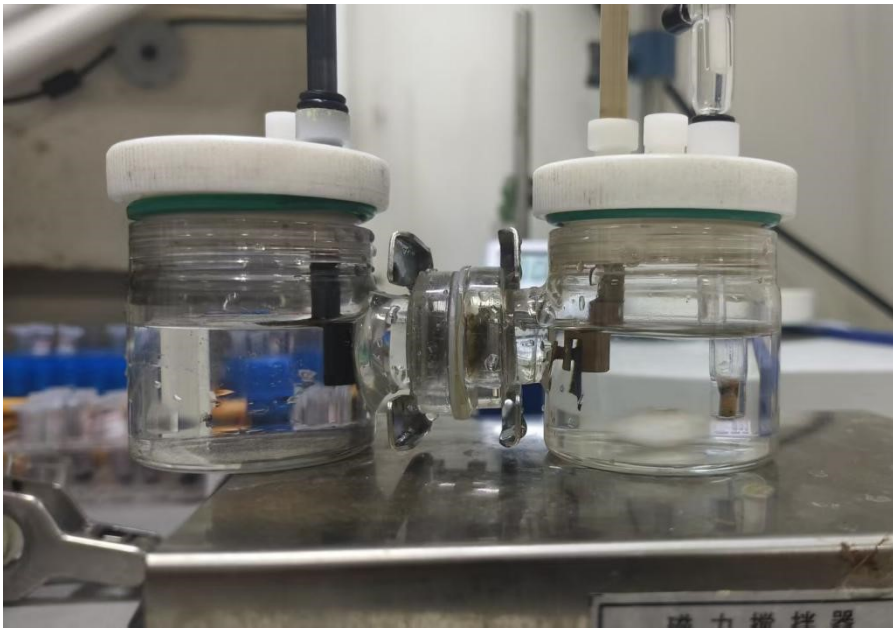

Fig. S3. H-type electrolysis cell equipped with Nafion 117 membrane.

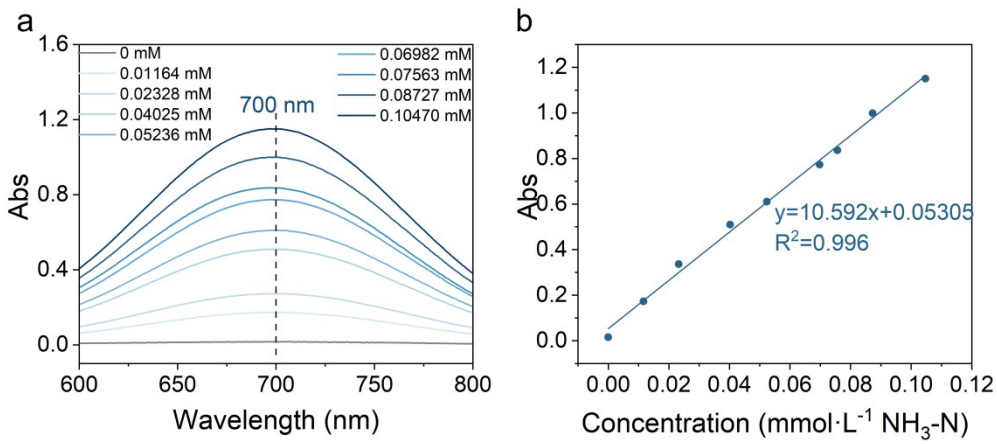

Fig. S4. (a) UV-Vis spectra of standard NH_3-N solutions with different concentrations; (b) the calibration curve of NH_3-N standard solutions.

NH_4Cl was used as the standard reference material, dissolved in a 0.1 M K_2SO_4 solution, and serially diluted to prepare standard solutions for constructing the calibration curve.

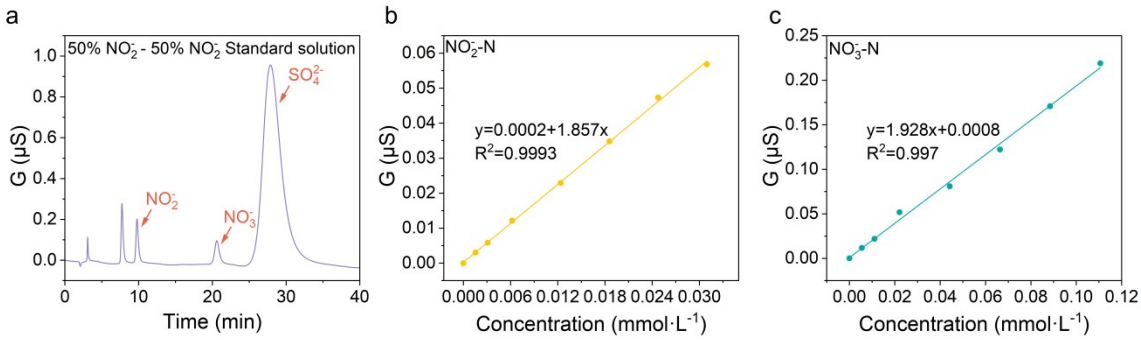

Fig. S5. (a) Elution profiles of analytes in ion chromatography, the standard curve of (b) NO_2^- concentration and (c) NO_3^- concentration.

The mixing solution containing 0.05 M SO_4^{2-}, 0.05 M NO_3^- and 0.05 M NO_2^- was used as the reference system to determine the retention times of various anions. The results showed the retention time ranges for NO_2^- (9.75 – 11.5 min), NO_3^- (20 – 24 min) and SO_4^{2-} (25 – 35 min). Due to the operational characteristics of the anion

chromatography system, certain anions such as SO_4^{2-} may exhibit some degree of deviation in peak appearance and retention time, which is considered normal.

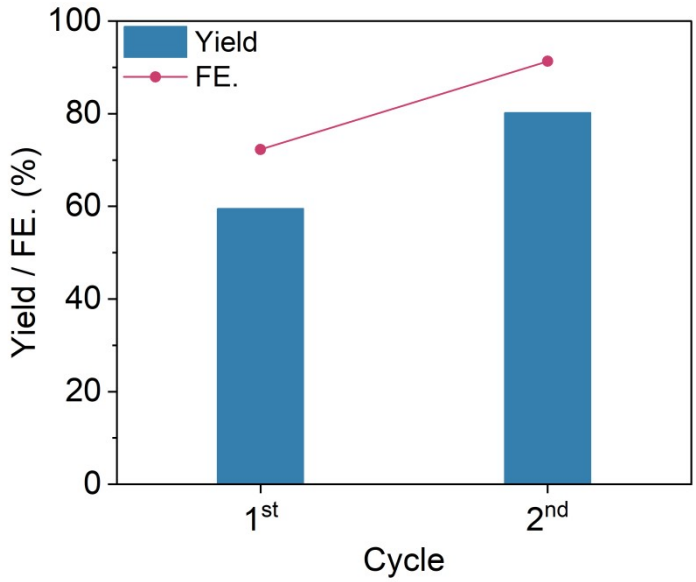

Fig. S6. NH_3 production performance in two cycles.

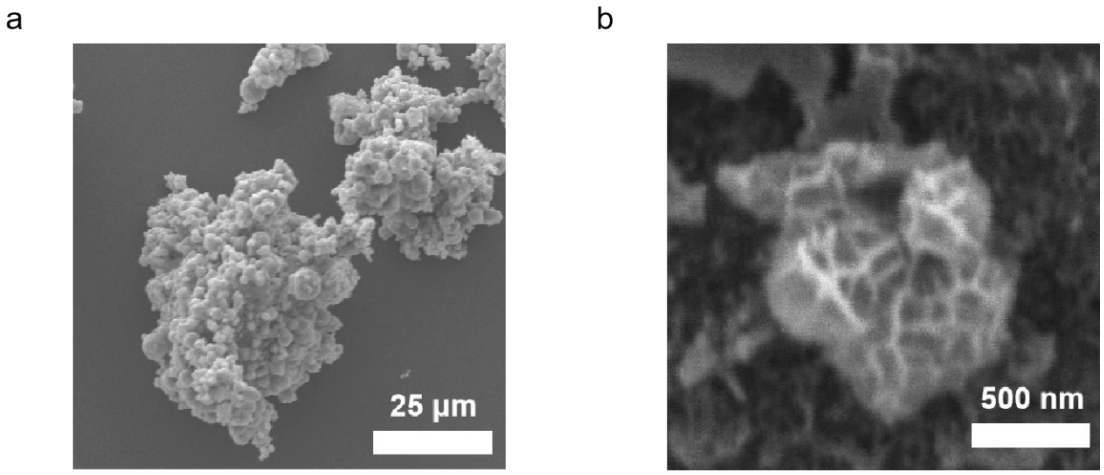

Fig. S7. SEM images of FeS_2 (a) before and (b) after the reaction.

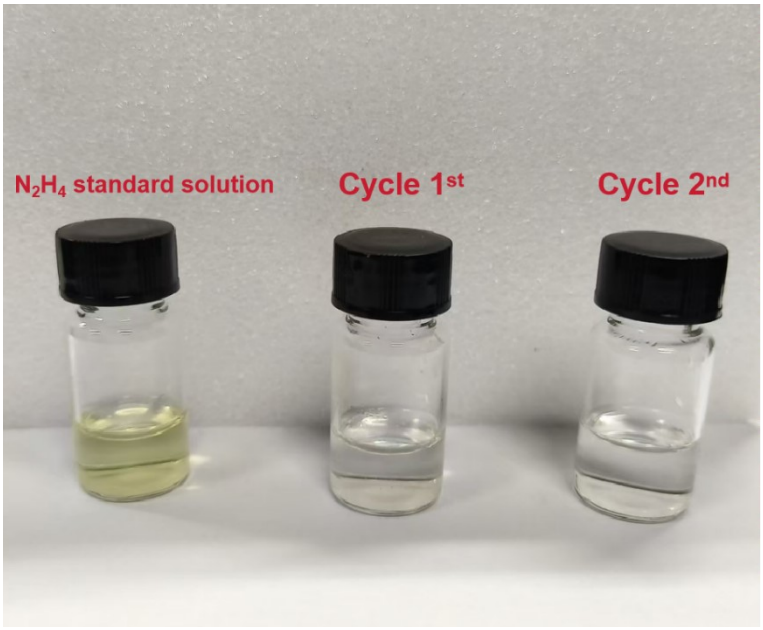

Fig. S8. N_2H_4 species showed coloration after two cycles.

From left to right are the color-developed hydrazine hydrate standard solution, the 1st-cycle reaction solution, and the 2nd-cycle reaction solution.

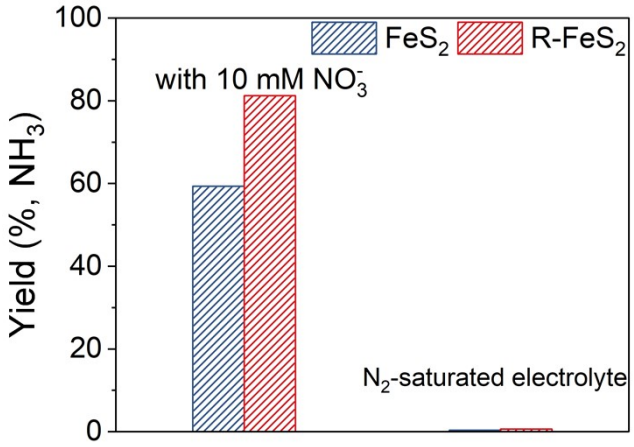

Fig. S9. N source screening of FeS_2 and S-FeOOH.

When nitrogen was introduced into the electrolyte without NO_3^- to saturate it, almost no NH_3 was produced compared to when KNO_3 was used as the substrate. This proved that NO_3^- was the sole nitrogen source for the reaction.

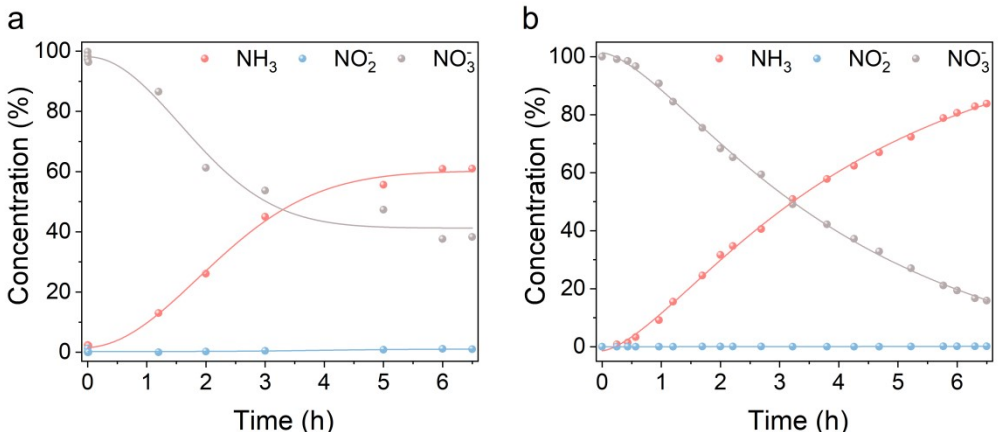

Fig. S10. The NH_3 yield was determined over two consecutive reaction cycles.

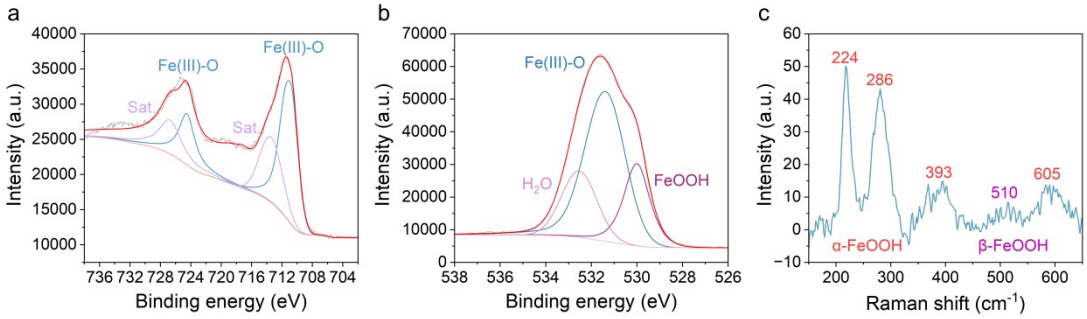

Fig. S11. XPS spectrum of (a) Fe 2p and (b) O 1s and (c) Raman spectrum of the synthesized FeOOH.

The reference sample of FeOOH was synthesized via a wet chemical method. The successful synthesis of FeOOH was confirmed by the characteristic Fe(III)–O lattice oxygen peak observed in the O 1s (**Fig. S16(b)**) at 528.0 – 532.0 eV, combined with Raman spectroscopy analysis. The synthesized FeOOH primarily consists of α-FeOOH, with a minor amount of β-FeOOH (approximately 535 cm^{-1}).[6, 7]

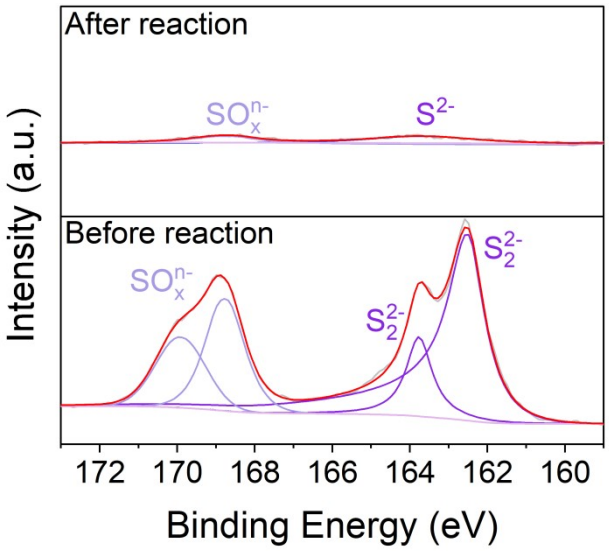

Fig. S12. XPS spectra of S 2p of FeS_2 before and after reaction.

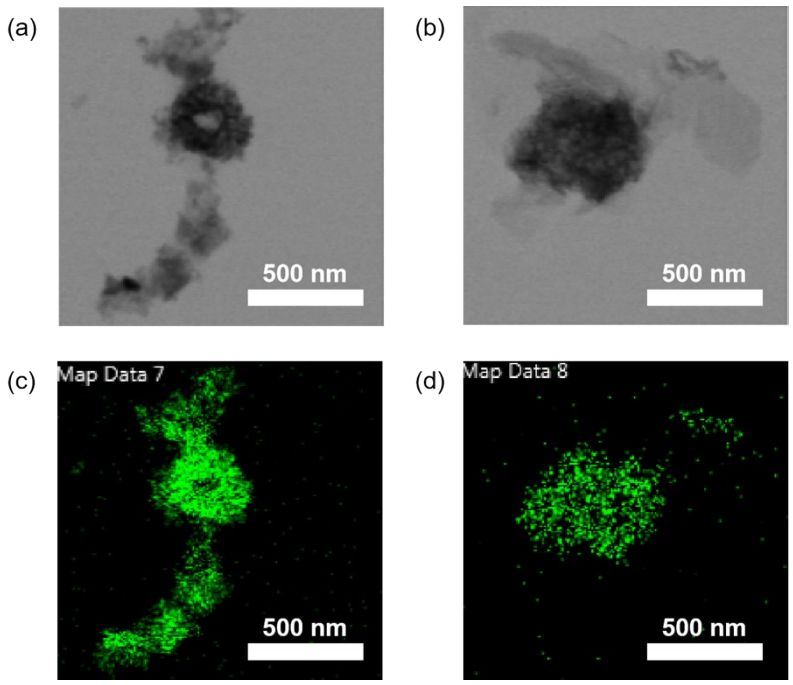

Fig. S13. TEM images of the catalyst (a) before and (b) after reaction, and EDS-mapping spectra of S species (c) before and (d) after reaction.

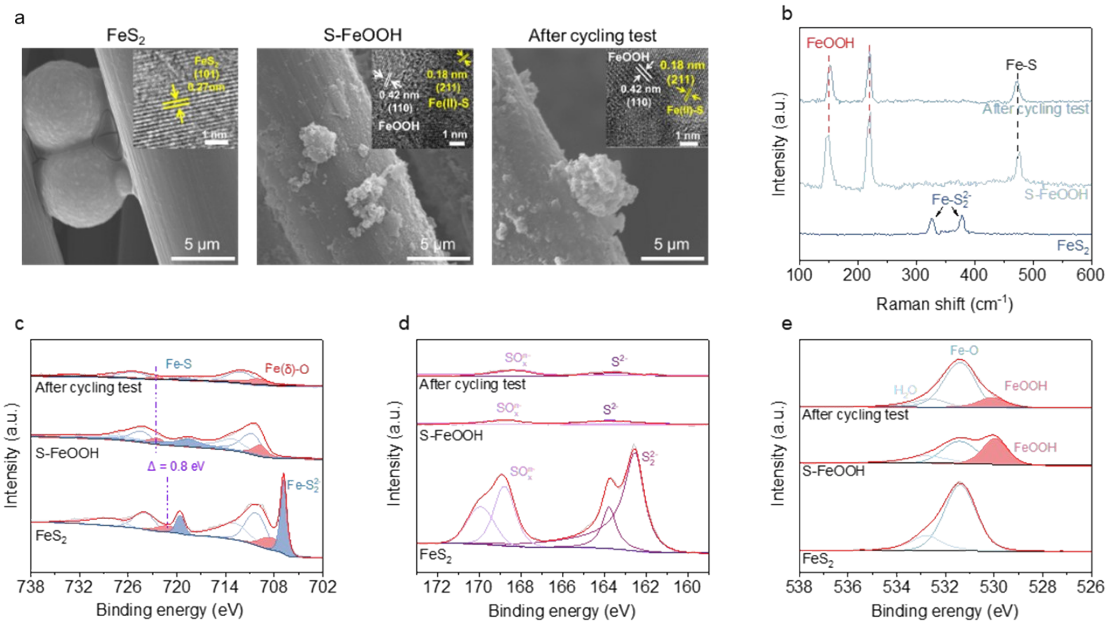

Fig. S14. (a) SEM images, (b) Raman spectrum, (c) Fe 2p, (d) S 2p and (e) O 1s XPS profiles of FeS_2, S-FeOOH and S-FeOOH after eNO_3RR cycling test. Insets of (a) are the corresponding TEM images.

The SEM and TEM observation identified that, unlike the spherical aggregation of FeS_2, S-FeOOH exhibits a nano-flower structure, and its morphology remained unchanged even after stability tests (**Fig. S14a**). Meanwhile, Raman investigation further confirmed that the S-FeOOH was well-remained after eNO_3RR cycling test (**Fig. S14b**), consistent with the slightly disappeared proportion of Fe-S_2^{2-} and intensity of S 2p with increasing proportion of FeOOH in O 1s identified by XPS (**Fig. S14c-e**). Therefore, S-FeOOH does not undergo further restructuring in subsequent reactions, even under external energy input or within the electrolyte micro-environment.

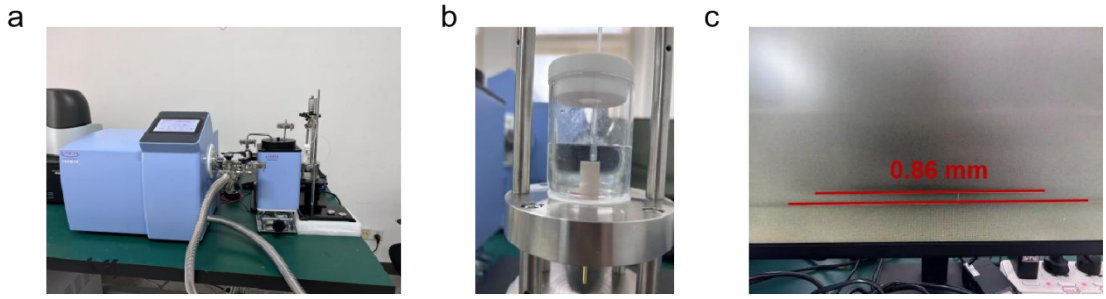

Fig. S15. DEMS equipment and its accompanying devices.

The distance from the electrode surface to the probe is 0.86 mm.

We adopted a glassy carbon electrode with FeS_2 drips (the surface specification of the electrode is 0.8 cm × 0.8 cm, and the load of FeS_2 is 0.4 mg) as the working electrode, Pt wire as the counter electrode, and Ag/AgCl electrode as the reference electrode. Use a mixture of 50 mL of 10 mM KNO_3 and 0.1 M K_2SO_4 as the electrolyte, and LSV scanning was performed on the catalyst of the load, with a scanning range of -1.7 to 0 V (vs. Ag/AgCl) and a scanning speed of 10 mV s^{-1}.

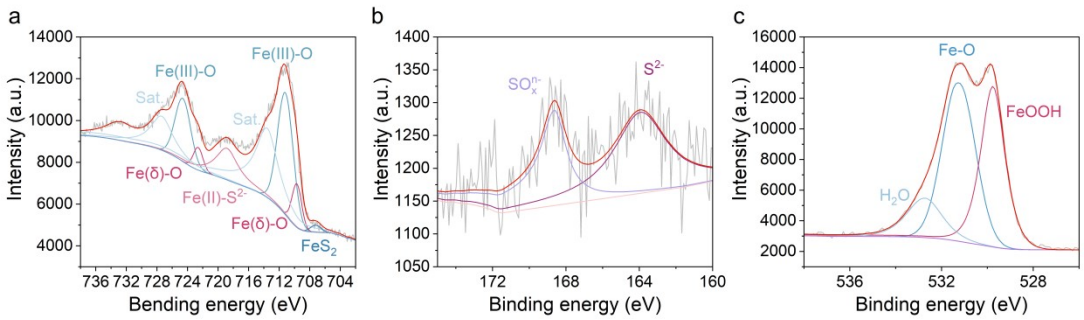

Fig. S16. XPS spectra of (a) Fe 2p (b) S 2p and (c) O 1s of FeS_2 after soaking in NO_3^-

.

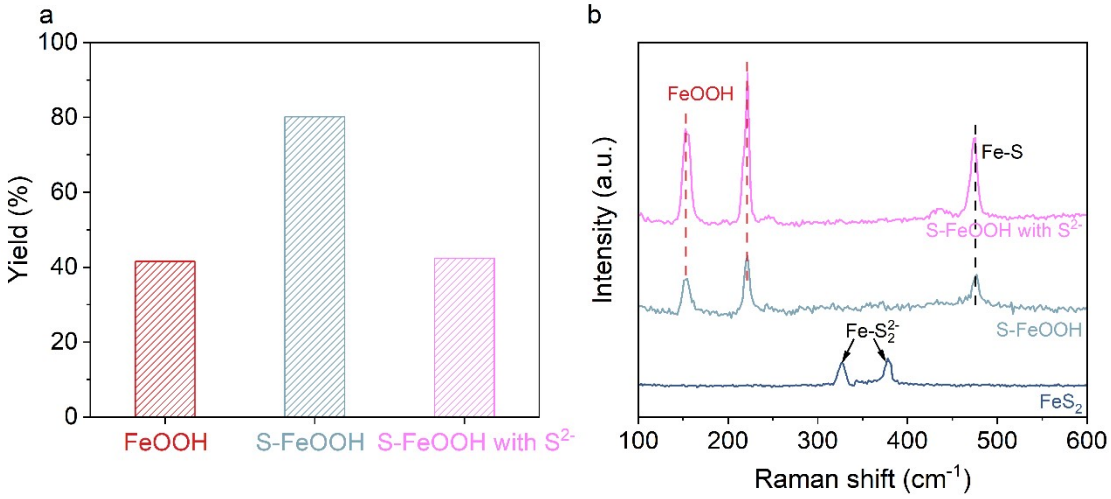

Fig. S17. (a) eNO_3RR performance and (b) Raman spectra of S-FeOOH reacting in 0.1 M K_2SO_4 without and with 66.7 ppm S^{2-}.

The eNO_3RR activity of S-FeOOH was assessed in an electrolyte containing 66.7 ppm S^{2-} (under the assumption that S_2^{2-} from FeS_2 underwent complete reconstitution and hydrolysis to S^{2-} or HS^-). The performance was comparable to that of FeOOH and nearly 40% inferior to that of pristine S-FeOOH, likely due to competitive adsorption between S^{2-} and NO_3^- at the catalytic interface. Structural analysis post-reaction revealed no characteristic FeS_2 peaks, confirming that the material retained the S-FeOOH structure and further substantiating the irreversibility of the spontaneous oxidative reconstitution process. Notably, the small peak (~470 cm^{-1}) likely arises from surface Fe-S species resulting from S^{2-} adsorption, where would prevent the exposure of the active site of S-FeOOH.

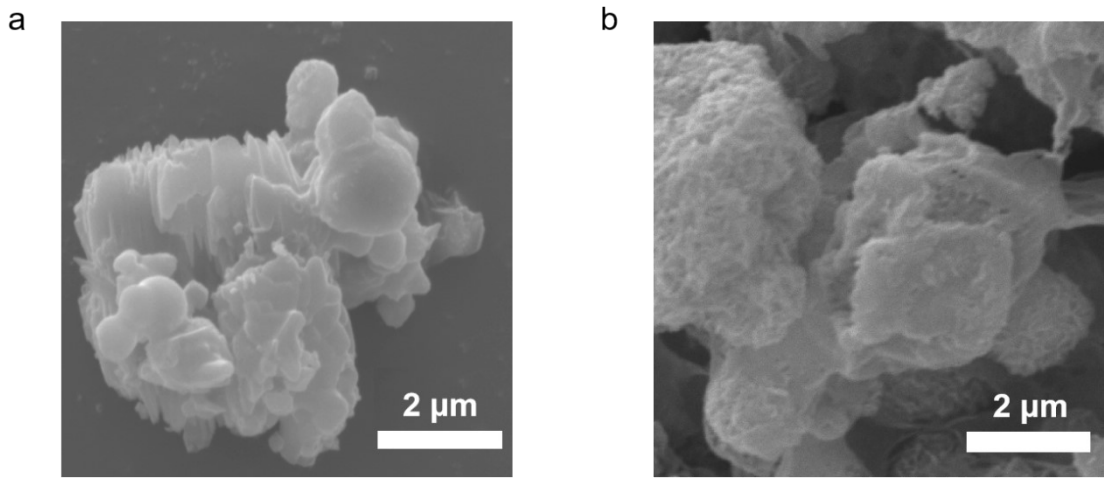

Fig. S18. SEM images of (a) initial FeS_2 and (b) simple after reaction in 0.1 M SO_4^{2-}.

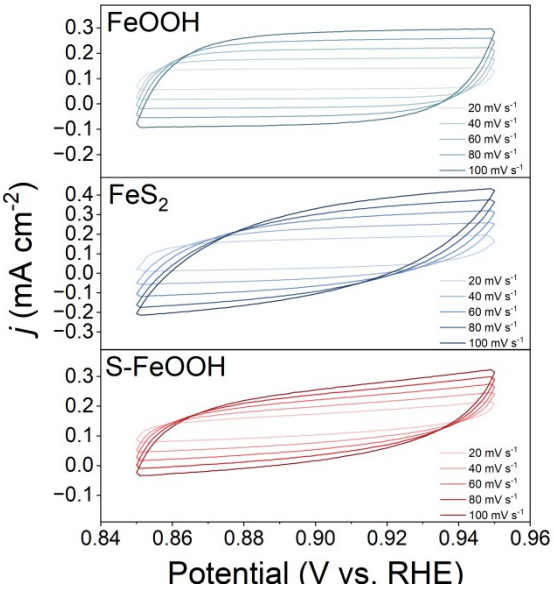

Fig. S19. CV spectra of Pure-phase FeOOH, FeS_2 and S-FeOOH at different scan rates.

Cyclic voltammetry (CV) was employed to investigate the evolution of active sites in the material. The measurements were conducted within a non-Faradaic window, and potential range of 0.85 - 0.95 V vs RHE at varying scan rates (20, 40, 60, 80, and 100 mV s^{-1}). The relative current density ($\Delta j=|j_a-j_p|/2$) at the intermediate potential of 0.90 V from the CV curves was plotted against the square root of scan rate .[8] Based on the work of Li and Hu, the electrochemical active surface area (ECSA) of the catalyst was calculated using a specific capacitance (C_s) of 40 μF·cm^{-2} to FeS_2 and FeOOOH.[9, 10]

The ECSA can be obtained according to the following equation:[11]

$$ECSA = \frac{C_{dl}}{C_s} \times S$$

C_s refers to the specific capacitance on the electrode surface or the capacitance of an atomically smooth planar surface of the material with 1 cm^2 of the real surface area,[3] and S is the actual area of the working electrode.

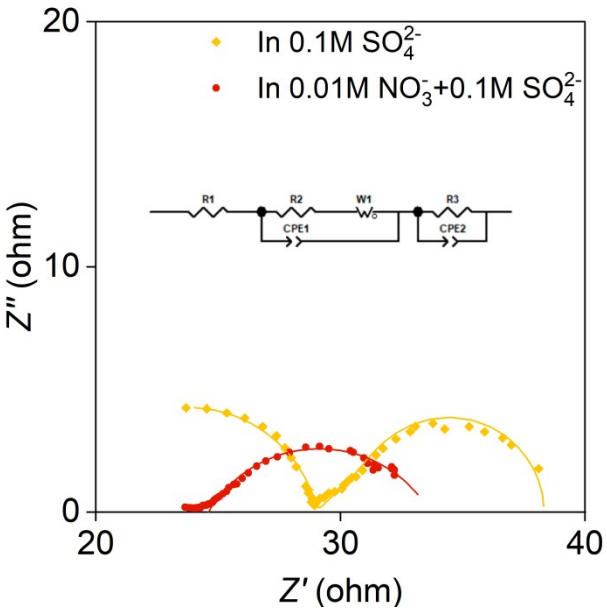

Fig. S20. Electrochemical impedance spectroscopy (EIS) diagrams of S-FeOOH in environments with or without NO_3^-.

The equivalent circuit model can be divided into three parts, which include the electrolyte resistance (R_1), the electron transfer from the cathode (catalyst inner-layer) to the reaction interface (R_2), and the interface reaction charge transfer involving electrochemical reactions (R_3) and diffusion (W_1).[3, 12]

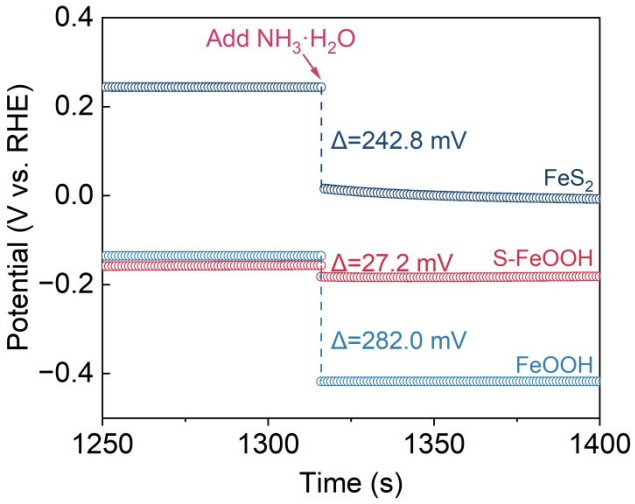

Fig. S21. Thermodynamic adsorption comparison of ammonia by FeS_2, S-FeOOH and FeOOH.

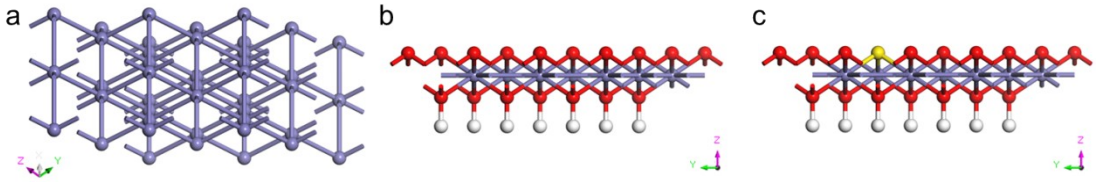

Fig. S22. The structural model of (a) Fe, (b) FeOOH and (c) S- FeOOH.

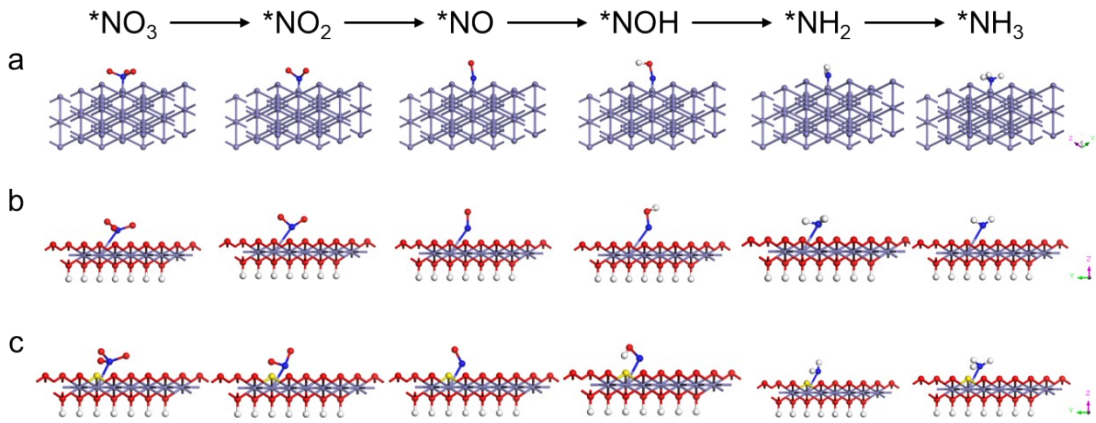

Fig. S23. The N species adsorption structure model of (a) Fe (b) FeOOH and (c) S-FeOOH.

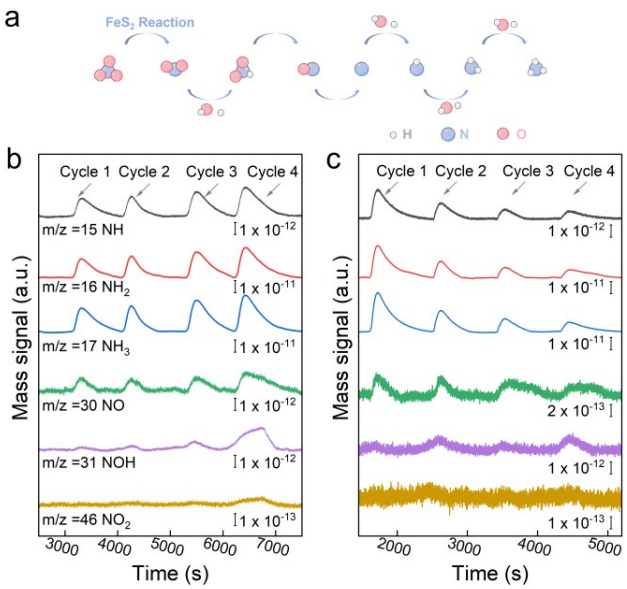

Fig. S24. (a) Schematic diagram of the reaction pathway. Electrochemical online DEMS results for eNO_3RR over the (b) S-FeOOH and (c) FeOOH.

According to previous work,[13-15] FeOOH and S-FeOOH both follow the simple path: $*NO_2$ - *NO - *NOH - *N - *NH - $*NH_2$ - $*NH_3$. Notably, signal of NOH (m/z = 31) enhanced on S-FeOOH while subsequent intermediates maintain stable, which demonstrates that the conversion from *NOH to *N is another rate-limiting step of eNO_3RR. The accumulated *NOH intermediates would hinder the electron transfer coupling on S-FeOOH, resulting the increase of the impedance at medium frequency region (0.1–1 Hz, **Fig. 4e**). In contrast, FeOOH shows weakened NH_3/NH_2 signals but enhanced NOH intensity, indicating hindered HNO to N conversion after multiple cycles. Therefore, suffering from *NOH surface accumulation, weak conversion of NO_3^- on FeOOH showed worse eNO_3RR than S-FeOOH.

Table S1. The electrocatalytic performance of NH_3 under different conditions.

Catalyst	Potential (V vs. RHE)	Yield (%)	FE. (%)
FeS_2	-0.80	58.36	72.36
FeS_2	No potential was applied	0.13	0
S-FeOOH	-0.80	80.23	93.73
Carbon cloth	-0.80	0	0

Table S2. Comparison of catalytic performance of FeS_2 with other reported NO_3RR electrocatalysts.

	Potential (V vs. RHE)	Electrolyte	FE. (%)	Reference
This work	-0.800	0.01 M KNO_3 + 0.10 M K_2SO_4	**93.7**	**This work**
Fe@Co	-0.785	1.20 mM $NaNO_3$ + 0.05 M Na_2SO_4	58.2	[16]
Fe SAC	-0.850	0.50 M KNO_3 + 0.10 M K_2SO_4	~75	[17]
CoO_x/Fe_3O_4-90	-0.900	0.10 M NO_3^- + 0.10 M KOH	82.22	[18]
Fe−CoS_2/CC	-0.900	0.10 M NO_3^- + 0.10 M Na_2SO_4	88.93	[19]
δ-FeOOH	-1.000	500 ppm NO_3^- + 0.25 M PBS	90.2	[6]
Fe−N/P−C	-0.400	0.10 M KNO_3 + 0.10 M KOH	90.3	[20]
F-Cu/Fe-Cu-60	-0.950	0.01 M NO_3^- + 0.10 M NaOH	91	[21]
Fe_2P	-0.550	0.20 M $NaNO_3$ + 0.50 M KOH	96	[22]

Table S3. the concentration of NO_2^- and S^{2-} in the soaking solution for different time.

[a] soak time (h)	[b] $C_{(NO2-)}$ ($\mu mol\ L^{-1}$)	[b] $C_{(S2-)}$ ($\mu mol\ L^{-1}$)	[c] S_2^{2-} : NO_2^-
0.5	7.3	29.8	2.04
1.0	16.5	65.3	1.98
3.0	19.8	76.3	1.93
6.0	19.9	79.2	1.99
12.0	19.6	77.9	1.99
24.0	19.7	78.2	1.98
48.0	20.0	78.9	1.97
72.0	20.1	79.3	1.97

[a] 0.042 mmol FeS_2 was soaked in 40 mL 0.1 M KNO_3.

[b] The retention time ranges for NO_2^- (9.75 – 11.5 min), NO_3^- (20 – 24 min) and S^{2-} (7 – 8 min).

[c] S_2^{2-} in solution was reduced to S^{2-} by 0.1 M $NaBH_4$.

Table S4. Reaction path of eNO_3RR

step of eNO_3RR	reaction path
1	$* + NO_3^- \rightarrow *NO_3$
2	$*NO_3 + H_2 \rightarrow *NO_2 + H_2O$
3	$*NO_2 + H_2 \rightarrow *NO + H_2O$
4	$*NO + 1/2\ H_2 \rightarrow *NOH$
5	$*NOH + 3/2\ H_2 \rightarrow *NH_2 + H_2O$
6	$*NH_2 + 1/2\ H_2 \rightarrow *NH_3$
7	$*NH_3 \rightarrow * + NH_3\ (g)$

Table S5. Calculated energy, entropy, zero-point energy correction and Gibbs free energy for eNO_3RR on Fe, FeOOH and S-FeOOH

catalyst	rection path	Δ*E* (eV)	ΔZPE (eV)	TΔ*S* (eV)	Δ*G* (eV)
Fe	* → *NO_3	-0.8	-2.6	1.3	-4.7
	*NO_3 → *NO_2	-1.6	0.9	0.4	-1.1
	*NO_2 → *NO	2.6	-1.9	0.3	0.4
	*NO → *NOH	-0.1	1.4	-0.2	1.5
	*NOH → *NH_2	-5.2	1.4	-1.5	-2.3
	*NH_2 → *NH_3	-0.5	-0.3	-0.1	-0.7
	*NH_3 → * + NH_3 (g)	-0.8	1.1	-0.2	0.5
FeOOH	* → *NO_3	-1.3	-0.6	-2.7	0.8
	*NO_3 → *NO_2	-1.5	-0.2	1.2	-1.3
	*NO_2 → *NO	2.2	-0.7	1.3	0.2
	*NO → *NOH	1.0	-0.7	-0.6	0.9
	*NOH → *NH_2	-7.8	1.4	-0.5	-5.9
	*NH_2 → *NH_3	-0.6	0.3	0.1	-0.4
	*NH_3 → * + NH_3 (g)	0.9	1.1	1.2	0.8
S-FeOOH	* → *NO_3	-1.9	-0.3	-1.9	-0.3
	*NO_3 → *NO_2	-1.2	-0.5	0.3	-2.0
	*NO_2 → *NO	2.2	-0.7	1.3	0.2
	*NO → *NOH	-0.5	-0.6	-1.4	0.3
	*NOH → *NH_2	-2.6	-0.7	0.8	-4.1
	*NH_2 → *NH_3	-0.2	-0.3	-0.3	-0.2
	*NH_3 → * + NH_3 (g)	-0.2	1.1	1.2	-0.3

References

1. A. Weiß, S. Schindler, S. Galbiati, M. A. Danzer and R. Zeis, *Electrochim. Acta*, 2017, **230**, 391-398.
2. J. Chen, E. Quattrocchi, F. Ciucci and Y. Chen, *Chem*, 2023, **9**, 2267-2281.
3. H. Fu, S. Lu, Y. Xin, S. Xiao, L. Chen, Y. Li and K. Shen, *Energy Environ. Sci.*, 2025, **18**, 818-830.
4. C. Guo, W. Zhou, X. Lan, Y. Wang, T. Li, S. Han, Y. Yu and B. Zhang, *J. Am. Chem. Soc.*, 2022, **144**, 16006-16011.
5. J. Sun, C. Liu, W. Kong, J. Liu, L. Ma, S. Li and Y. Xu, *J Mater Sci Technol*, 2022, **110**, 161-166.
6. K. Qu, X. Zhu, Y. Zhang, L. Song, J. Wang, Y. Gong, X. Liu and A. L. Wang, *Small*, 2024, **20**, 2401327.
7. J. Hu, S. Li, J. Chu, S. Niu, J. Wang, Y. Du, Z. Li, X. Han and P. Xu, *ACS Catal.*, 2019, **9**, 10705-10711.
8. S. A. Kadam, D. P. Jaihindh, Y.-R. Chen, K. P. Kadam, H.-W. Hsieh, S. Bera, S. Kc, A. V. Sumant, Y.-P. Fu, C.-C. Lai, Y.-R. Ma and N. R. Pradhan, *ACS Appl. Nano Mater.*, 2024, **7**, 27566-27578.
9. H. Li, X. Song, N. Zhang, K. Chu and J. Zhao, *J. Colloid Interface Sci.*, 2025, **678**, 242-250.
10. Y. Hu, Y. Ji, F. Ren, S. Tan and J. Yao, *J. Mater. Sci.*, 2022, **57**, 17577-17591.
11. J. Tan, L. Feng, J. Shao, W. Zhang, H. Qin, H. Liu, Y. Shu, L. Yang, Y. Meng, Y. Tang and Q. Gao, *J. Am. Chem. Soc.*, 2025, **147**, 10118-10128.
12. Q.-L. Hong, B. Sun, X. Ai, X.-L. Tian, F.-M. Li and Y. Chen, *Adv. Funct. Mater.*, 2024, **34**, 2310730.
13. W. Ye, Y. Zhang, L. Chen, F. Wu, Y. Yao, W. Wang, G. Zhu, G. Jia, Z. Bai, S. Dou, P. Gao, N. Wang and G. Wang, *Angew. Chem. Int. Ed.*, 2024, **63**, e202410105.
14. R. Zhang, X. Ma, S. Zhang, Q. Li, Y. Zhao and C. Zhi, *ChemElectroChem*, 2025, **12**, e202400499.
15. X. Gu, J. Zhang, S. Guo, Y. Zhang, L. Xu, R. Jin and G. Li, *J. Am. Chem. Soc.*, 2025, **147**, 22785−22795.
16. I. Kuznetsova, O. Lebedeva, D. Kultin, M. Mashkin, K. Kalmykov and L. Kustov, *Int. J. Mol. Sci.*, 2024, **25**, 7089.
17. Z.-Y. Wu, M. Karamad, X. Yong, Q. Huang, D. A. Cullen, P. Zhu, C. Xia, Q. Xiao, M. Shakouri, F.-Y. Chen, J. Y. Kim, Y. Xia, K. Heck, Y. Hu, M. S. Wong, Q. Li, I. Gates, S. Siahrostami and H. Wang, *Nat. Commun.*, 2021, **12**, 2870.
18. Y. Zhou, H. Sun, X. Hu, J. Guo, Y. Liang, X. Gong, X. Xiao, L. Luo, Z. Wu and P. Qin, *J. Colloid Interface Sci.*, 2025, **683**, 709-721.
19. X. Lu, J. Zhou, J. Zhao, D. Wu, X. Liu, X. Ren, Q. Wei and H. Ju, *ChemPhysChem*, 2023, **24**, e202300536.
20. J. Xu, S. Zhang, H. Liu, S. Liu, Y. Yuan, Y. Meng, M. Wang, C. Shen, Q. Peng and J. Chen, *Angew. Chem. Int. Ed.*, 2023, **135**, e202308044.
21. Y. Wang, Y. Ran, C. Qiu, W. Hu and T. Li, *Appl. Mater. Today*, 2025, **42**, 102536.
22. T. Chouki, M. Machreki, I. A. Rutkowska, B. Rytelewska, P. J. Kulesza, G. Tyuliev, M. Harb, L. M. Azofra and S. Emin, *J. Environ. Chem. Eng.*, 2023, **11**, 109275.